Physics in Medicine & Biology

IPEM Institute of Physics and Engineering in Medicine

PAPER

Measurement of PET isotope production cross sections for protons and carbon ions on carbon and oxygen targets for applications in particle therapy range verification

Felix Horst[1,2], Wihan Adi[1,3], Giulia Aricò[4], Kai-Thomas Brinkmann[3], Marco Durante[2,5], Claire-Anne Reidel[2,6], Marta Rovituso[7,8], Uli Weber[2], Hans-Georg Zaunick[3], Klemens Zink[1,9,10] and Christoph Schuy[2,11]

1   Institute of Medical Physics and Radiation Protection (IMPS), THM University of Applied Sciences Giessen, 35390 Giessen, Germany
2   GSI Helmholtzzentrum für Schwerionenforschung, 64291 Darmstadt, Germany
3   II. Physics Institute, Justus Liebig University, 35392 Giessen, Germany
4   European Organization for Nuclear Research (CERN), 1211 Geneva, Switzerland
5   TU Darmstadt, 64289 Darmstadt, Germany
6   Université de Strasbourg, CNRS, IPHC UMR 7871, 67000 Strasbourg, France
7   Trento Institute for Fundamental Physics and Applications (TIFPA), 38123 Povo Trento, Italy
8   HollandPTC, 2629 Delft, The Netherlands
9   Department of Radiotherapy and Radiooncology, University Medical Center Giessen-Marburg, 35043 Marburg, Germany
10 Frankfurt Institute for Advanced Studies (FIAS), 60438 Frankfurt am Main, Germany
11 Author to whom correspondence should be addressed.

E-mail: c.schuy@gsi.de

Abstract

Measured cross sections for the production of the PET isotopes ^{10}C, ^{11}C and ^{15}O from carbon and oxygen targets induced by protons (40–220 MeV) and carbon ions (65–430 MeV u^{-1}) are presented. These data were obtained via activation measurements of irradiated graphite and beryllium oxide targets using a set of three scintillators coupled by a coincidence logic. The measured cross sections are relevant for the PET particle range verification method where accurate predictions of the β^+ emitter distribution produced by therapeutic beams in the patient tissue are required. The presented dataset is useful for validation and optimization of the nuclear reaction models within Monte Carlo transport codes. For protons the agreement of a radiation transport calculation using the measured cross sections with a thick target PET measurement is demonstrated.

1. Introduction

Radiotherapy with protons and heavy ions (*particle therapy*) has many potential advantages over conventional techniques using high energy photons or electrons. Besides radiobiological aspects, most of these advantages arise from the highly localized energy deposition pattern of heavy charged particles due to their electromagnetic interaction properties. These lead to the Bragg peak at the end of the particle range and in the case of heavy ions to a sharp lateral dose fall-off even at large depths. This allows for a better tumor conformity together with good sparing of healthy tissues (Schardt *et al* 2010, Newhauser and Zhang 2015). However, along with this high precision comes also a high sensitivity of the dose distributions against several different factors like anatomical changes, imaging artifacts or inaccuracies in the conversion from HU values to stopping power ratio (relative to water) (Knopf and Lomax 2013). The particle range uncertainties resulting from these influences are among the major critical problems in modern particle therapy. Therefore, a reliable method to verify the range predicted by the treatment planning system, either directly during the treatment (*online*) or between two fractions (*offline*), would be highly beneficial to better exploit the full potential of particle therapy. Eventually, a fully developed range verification method could lead to reduced safety margins around the treatment volume and thus improve particle therapy in general.

Different methods have been proposed to achieve this goal (Parodi and Polf 2018). Most of them are based on the nuclear reactions which occur between the projectiles and the nuclei within the patient body (Durante and

Paganetti 2016). For instance, for one proposed technique long range secondary fragments escaping the body of a patient irradiated with carbon ions are tracked and back projected into the patient (Henriquet *et al* 2012, Gwosch *et al* 2013, Piersanti *et al* 2014, Muraro *et al* 2016). Among such techniques in an experimental stage, especially the detection of prompt gamma photons seems very promising for both proton (Min and Kim 2006, Smeets *et al* 2012) and carbon ion therapy (Testa *et al* 2009) and first clinical prototypes have already been built (Richter *et al* 2016, Hueso-Gonzalez *et al* 2018). However, the only method which up to now has proven to be suitable for routine operation during patient treatments is particle therapy positron emission tomography (PT-PET), where the spatial distribution of positron emitting nuclear fragments (e.g. ^{15}O, ^{11}C or ^{10}C) is measured using a PET camera (Bennett *et al* 1975), either in-beam (Enghardt *et al* 1999, Parodi *et al* 2002, Fiorina *et al* 2018), in-room (Nishio *et al* 2010, Zhu *et al* 2011) or offline (Parodi *et al* 2007, Combs *et al* 2012). The measured positron emitter activity distribution produced along the beam path is compared with the prediction calculated for the individual treatment plan with a suitable radiation transport code. The treatment delivery can be considered range-error-free if the measured activity pattern matches the calculated one. Effects that also have to be considered are the biological washout of the generated isotopes and the resolution of the PET-scanner used. In addition to these factors, the sensitivity of the method depends strongly on the accuracy of the nuclear reaction models within the radiation transport code used (Bauer *et al* 2013, Lühr *et al* 2014) because uncertainties in the prediction of the positron emitter yields may cause deviations between measurement and calculation even if the treatment is delivered without any range errors. Major errors in the irradiation (e.g. irradiation through an empty sinus instead of a filled one as described by Enghardt *et al* (2004)) can already be well detected with the PT-PET method using radiation transport codes in their current state. By further optimizing the nuclear reaction models predicting the positron emitter production also smaller errors might become detectable and the clinically desired millimeter accuracy could be reached (Espana *et al* 2011, Lühr *et al* 2014). However, the available experimental cross section data for the relevant reaction channels at high energies are scarce (Nichols and Capote 2014).

In this work proton and carbon ion cross section data for the optimization of radiation transport codes for PT-PET applications are presented. Cross sections for the production of ^{10}C, ^{11}C and ^{15}O target fragments in collisions of protons (40–220 MeV) and carbon ions (65–430 MeV u^{-1}) with carbon and oxygen targets were measured during experiments conducted at the Marburger Ionenstrahl-Therapiezentrum (MIT).
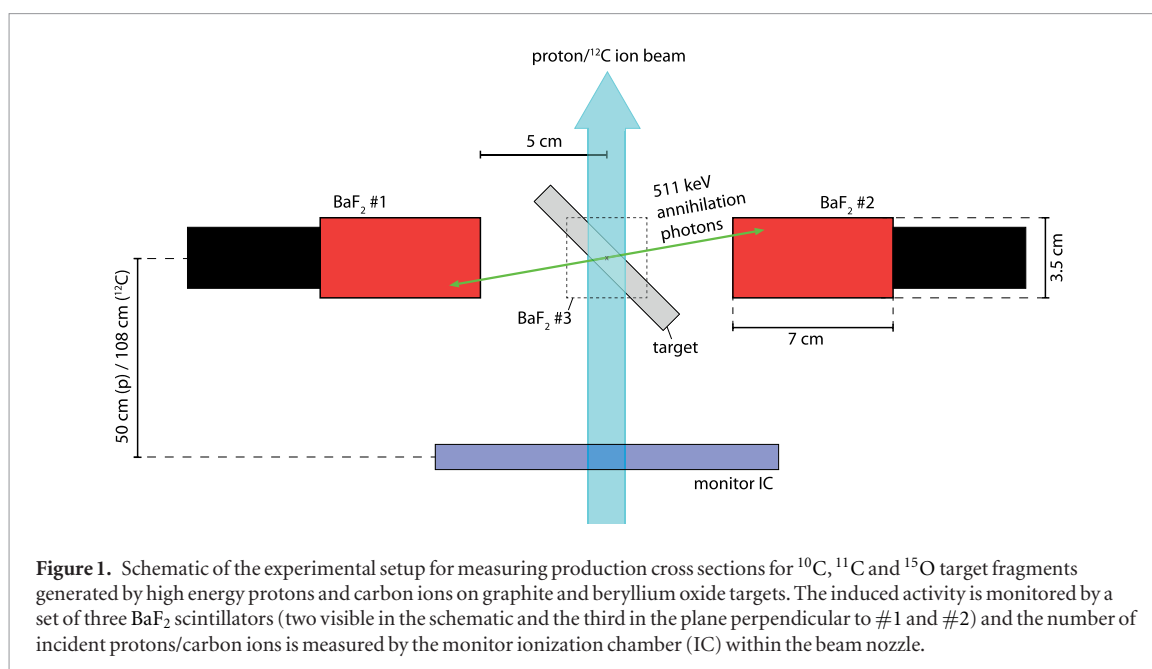
Graphite or beryllium oxide targets were activated by short intense proton or carbon ion pulses and the subsequent β^+-decay of the generated target fragments (^{11}C and ^{10}C in graphite plus ^{15}O in beryllium oxide) was monitored by measuring the 511 keV annihilation photon pairs emitted at the characteristic angle of 180°. Random coincidences were measured at an angle of 90° and subtracted from the 180° coincidences to obtain the true coincidence rate. The initial count rates of the produced ^{10}C (half life: 19.29 s), ^{11}C (half life: 20.334 min) and ^{15}O (half life: 122.24 s) were obtained by fitting the measured decay curves with a composite exponential decay function. These initial count rates could be converted into initial activities by considering the detection efficiency, which had to be calculated separately for each measurement. The production cross sections for the individual isotopes could then be derived from the measured initial activities, the target thickness and the number of primary protons/ions impinging on the target. The obtained cross sections are compared with exisiting literature data and their importance for nuclear reaction modeling is discussed. Furthermore a radiation transport calculation for a tissue equivalent phantom irradiated with protons was performed using the measured cross sections as input. The results are in good agreement with a PET-based measurement of the activity profiles reported in the literature.

2. Materials and methods

2.1. The measurement concept

The method for the measurement of PET isotope production presented in this work is conducted in the several steps, described in the following: the experimental setup, consisting of three scintillators and a coincidence unit is positioned at the beamline and aligned according to the laser positioning system. The next step is a calibration measurement using a ^{22}Na point source with known activity positioned at the center of the detection system guided by the positioning lasers. To be able to calculate the detection efficiency properly, the beamspot has to be characterized before the actual activation measurement can be performed. For this purpose, a Gafchromic EBT3 film is positioned in the target holder and the laser markings are transfered to the film before it is irradiated by a short pulse of protons or ions with the same beam settings used for the activation measurement later. Finally, the irradiated film is exchanged with the target, the data acquisition system is turned on and the target is irradiated. The induced β^+ activity can then be monitored as long as necessary (typically 15–30 min depending on the isotopes of interest) and afterwards the next measurement can be performed.

In this section each of the above mentioned steps and components are described in detail.

Figure 1. Schematic of the experimental setup for measuring production cross sections for ^{10}C, ^{11}C and ^{15}O target fragments generated by high energy protons and carbon ions on graphite and beryllium oxide targets. The induced activity is monitored by a set of three BaF$_2$ scintillators (two visible in the schematic and the third in the plane perpendicular to #1 and #2) and the number of incident protons/carbon ions is measured by the monitor ionization chamber (IC) within the beam nozzle.

2.2. Experimental setup

A schematic of the experimental setup is shown in figure 1.

Three BaF$_2$ scintillators (crystal dimensions: $3.5 \times 3.5 \times 7$ cm^3) with a thin wrapping and a Hamamatsu R1668 photomultiplier are arranged around a thin graphite or beryllium oxide target tilted by 45°. The BaF$_2$ scintillators are positioned at a distance of 5 cm from the target center. Two of them (#1 and #2) are arranged at 180° to measure the coincidence rate of the 511 keV annihilation photons following the β^+ decays and a third one (#3) is arranged at 90° to measure the random coincidence rate. The targets and films are positioned in a 3D-printed holder with a modular setup and can easily be exchanged without affecting the detector setup.
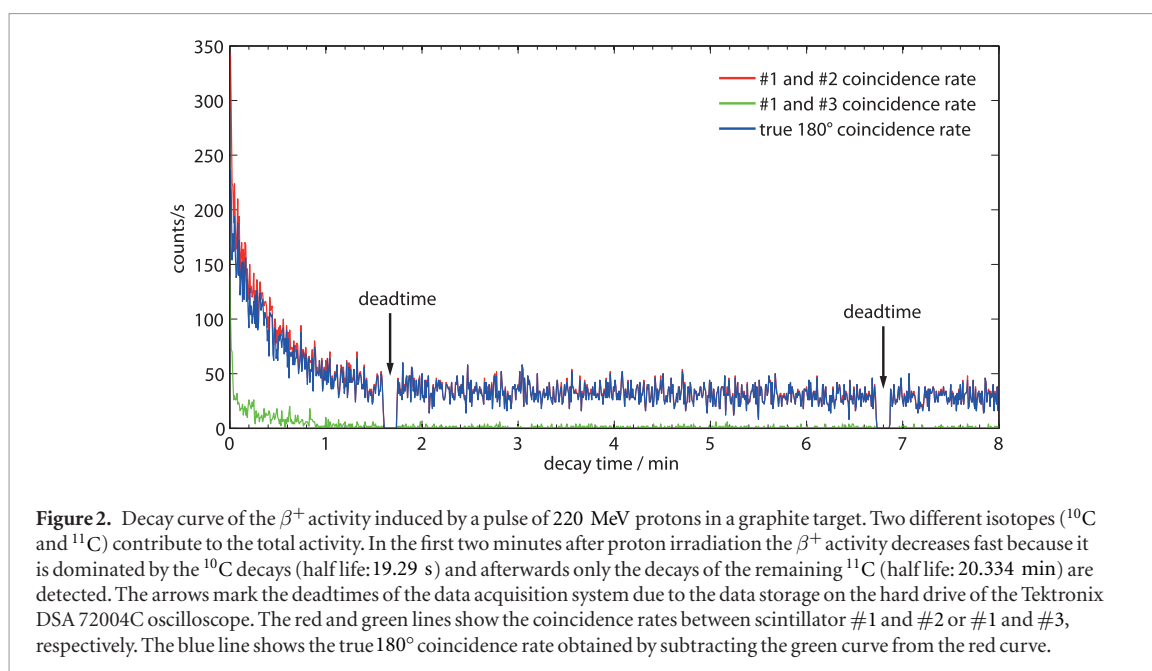
2.3. Beam application

The irradiations were performed as treatment plans with a single beam spot. The raster scanning control system monitored the irradiation and the number of incident particles measured by the monitor IC within the nozzle was documented in the machine records. All irradiations were done using the beam line settings for the smallest focus (FWHM at the isocenter: 8.1–30.5 mm for protons and 3.4–9.3 mm for carbon ions) and at the highest intensity that can be extracted from the synchrotron ($1.5 \cdot 10^9$ protons s^{-1} and $6.5 \cdot 10^7$ carbon ions s^{-1}). The beam pulses had a duration of ~1.3 s for protons and ~1.0–2.5 s for carbon ions. These short pulse durations were chosen to ensure that the time of isotope production was well defined and small against the decay times. The number of particles per measurement were $1.9 \cdot 10^9$ for protons and between $6.5 \cdot 10^7$ and $1.9 \cdot 10^8$ for carbon ions.

2.4. Coincidence trigger and data acquisition

The trigger unit was built from a set of NIM modules (discriminator, gate generator, coincidence module, dual timer) and generated a trigger signal for coincident signals either from detector #1 and #2 (180°) or from detector #1 and #3 (90°). The coincidence window was adjusted to 30 ns, which provided a good noise suppression for the 180° scintillator pair. However, there was still the possibility to measure random coincidences caused by two independent β^+ decays that occur both within the coincidence window. This random coincidence rate was monitored by the 90° scintillator pair. Subtracting the coincidence rate measured by detector #1 and #3 from the rate measured by #1 and #2 gives the *true* 180° coincidence rate as shown in figure 2.

This example shows that the random coincidence rate strongly depends on the present activity. In the time shortly after the irradiation, when the activity is at its maximum, random coincidences contribute more than 30% to the total coincidences measured at 180°. However, as the activity decreases, after ~2 min the contribution of random coincidences to the total coincidence rate subsides significantly.

A Tektronix DSA 72004C oscilloscope was used for data acquisition. The signals of the three scintillators were recorded as waveforms by means of fast sampling (sample rate 3.1 GS s^{-1}) triggered by the coincidence unit. The oscilloscope can store data in its RAM with low deadtime between consecutive events, but every few 1000 events (depending on the exact acquisition settings like sample rate or digital resolution) it needs to save the stored data on a hard drive. During these few seconds, the oscilloscope does not accept any triggers which causes a gap in the measured decay curves every few minutes. Examples of such storage deadtimes are marked by arrows in figure 2.

Figure 2. Decay curve of the β^+ activity induced by a pulse of 220 MeV protons in a graphite target. Two different isotopes (^{10}C and ^{11}C) contribute to the total activity. In the first two minutes after proton irradiation the β^+ activity decreases fast because it is dominated by the ^{10}C decays (half life: 19.29 s) and afterwards only the decays of the remaining ^{11}C (half life: 20.334 min) are detected. The arrows mark the deadtimes of the data acquisition system due to the data storage on the hard drive of the Tektronix DSA 72004C oscilloscope. The red and green lines show the coincidence rates between scintillator #1 and #2 or #1 and #3, respectively. The blue line shows the true 180° coincidence rate obtained by subtracting the green curve from the red curve.

In an offline analysis the 511 keV peaks were separated by applying a cut on the energy spectra. In order to suppress the measurement of prompt gamma photons which are produced during the irradiation, the end-of-plan signal from the accelerator control system was used to start the data acquisition immediately after the end of the spill (the trigger pulse is created 120 ms after the end of beam extraction). Furthermore, the end-of-plan signal was used to precisely determine the time when the beam pulse ended.
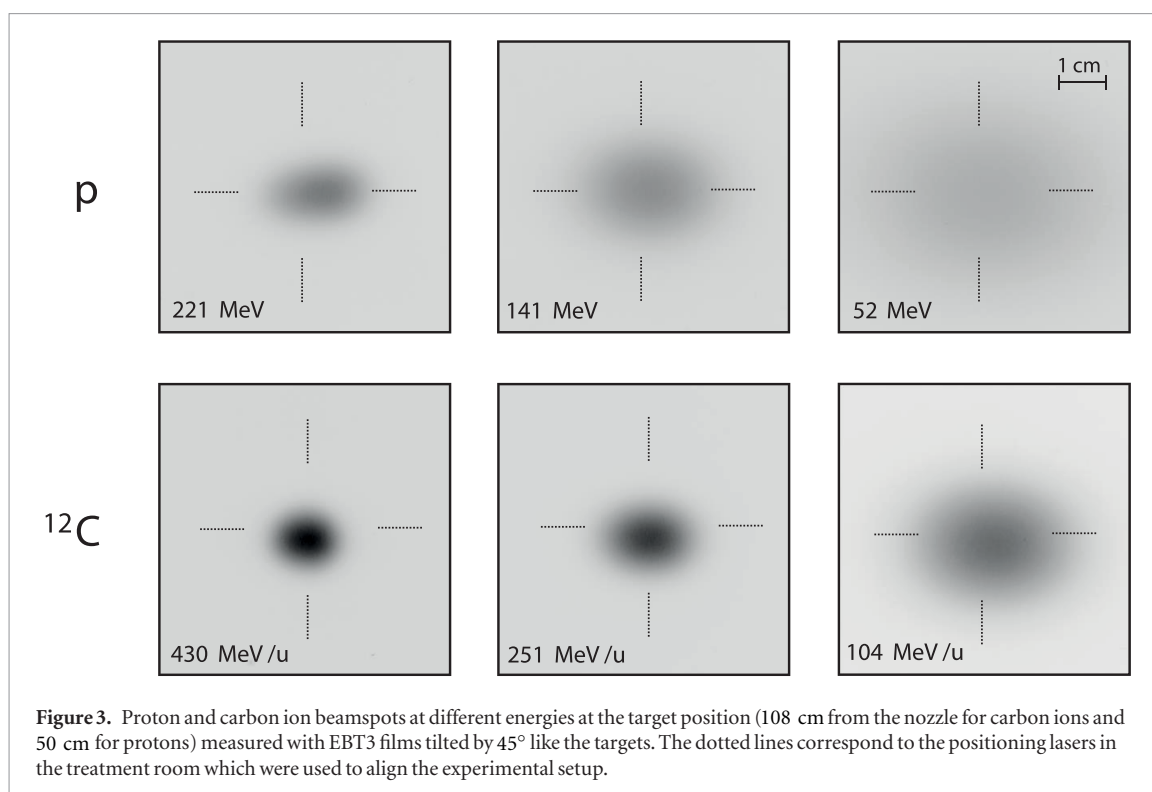
2.5. Targets

Two different target materials were irradiated in the present experiments. To obtain the production cross sections for the isotopes ^{10}C and ^{11}C on carbon, graphite targets (SGL Carbon R 6550, density: 1.83 g cm^{-3}) with thicknesses of 5 mm and 10 mm (depending on the beam energy) and lateral dimensions of 80×80 mm^2 were irradiated with protons and carbon ions. To obtain the production cross sections for ^{15}O on oxygen, beryllium oxide targets (Materion Thermalox 995, density: 2.85 g cm^{-3}) with a thickness of 3.9 mm and lateral dimensions of 114×114 mm^2 were used. For the measurements presented in this work (production of positron emitters) beryllium oxide acts as a pure oxygen target because the beryllium does not fragment into β^+-isotopes (as discussed by Tobias *et al* (1971)) and therefore does not contribute to the measured activity. To enhance the efficiency of the detection system, the targets were tilted by 45° (see figure 1). The local roughness at the center of the targets (uncertainty of the thickness) was <1%.

2.6. Beamspot characterization

The calculation of the detection efficiency (as described in the next section) relies on the knowledge of the spatial distribution of the induced β^+ radioactivity within the target relative to the detectors. To estimate the activity distribution within the target for each individual species-energy-target combination, fluence measurements using EBT3 films located exactly at the target position (also with the 45° tilt) were performed in advance before all target irradiations. From these films measured vertical and horizontal fluence profiles were obtained and fitted with single gaussian functions to be used for the calculation of the efficiency (see section 2.7). Also shifts of the beamspots relative to the scintillator setup could be detected and taken into account for the efficiency calculation. The parameters characterizing a beamspot are called FWHM$_{horizontal}$, FWHM$_{vertical}$, $shift_{horizontal}$ and $shift_{vertical}$.

To convert the grey values of the EBT3 films into fluence values, a calibration function was determined for both protons and carbon ions. Carbon ion measurements were restricted to the isocenter (distance from isocenter to nozzle: ~108 cm) where the beamspot sizes are daily checked and documented in the QA protocols. For the proton irradiations the setup was moved to a distance of 50 cm from the nozzle. This closer distance was of advantage especially for the low proton energies because proton beams scatter much stronger within the nozzle (~2 mm water equivalent thickness) than carbon ion beams, which leads to relatively large proton beamspots at the isocenter (see above).

Figure 3 shows examples of films irradiated with protons and carbon ions. As expected the carbon ion beamspots are sharper compared to the proton beamspots. The beam spot sizes get larger for lower energies due to the increased lateral scattering within the nozzle. Slight shifts of the beamspots relative to the positioning lasers can be observed depending on the energy. The film response to the carbon ions is stronger than to protons due to

Figure 3. Proton and carbon ion beamspots at different energies at the target position (108 cm from the nozzle for carbon ions and 50 cm for protons) measured with EBT3 films tilted by 45° like the targets. The dotted lines correspond to the positioning lasers in the treatment room which were used to align the experimental setup.

their higher LET. The beamspots appear stretched in horizontal direction because the films were irradiated with the 45° tilt like the targets.

2.7. Efficiency calculation

For the calculation of the production cross sections for the different isotopes, their absolute activities produced by the proton or ion pulses within the targets need to be determined. For such an absolute measurement the efficiency of the detection system (count rate per activity) must be known. Because the beamspot sizes and therefore the spatial distribution of the induced radioactivity varied considerably among the different beams used (see figure 3), the efficiency had to be determined for each measurement separately.

To calculate the detection efficiency for each individual measurement, a numerical algorithm was developed which takes all relevant effects into account: the detection efficiency depends (a) on the spatial distribution of the β^+ activity relative to the detector setup (for activities located in the center the efficiency is maximum and drops at the sides), (b) on the amount of material between the activity and the detectors (causing attenuation of the 511 keV annihilation photons) and (c) on the distance between the activity and the target edge (positrons may escape from the target and annihilate outside the detection zone).

The efficiency algorithm requires the following input parameters: the first parameter is the maximum efficiency of the detection system determined with a ^{22}Na point source with known activity positioned at the center of the detection zone. This calibration was repeated each time the experiment was re-built to take account of e.g. small variations in the electronic thresholds of the coincidence unit or a slight geometrical misalignment of the detectors. Secondly, the beamspot parameters ($FWHM_{horizontal}$, $FWHM_{vertical}$, $shift_{horizontal}$, $shift_{vertical}$) obtained from the film measurement have to be taken into consideration to model the activity distribution in the target. Lastly, the target thickness and material have to be specified to enable an accurate estimation of the photon (self-) absorption and the fraction of positrons that escape the target without annihilation.

Based on the beamspot parameters, the algorithm models the spatial distribution of the β^+ radioactivity within the target divided into voxels (80×80 voxels lateral and 100 voxels in depth) considering that the induced activity is proportional to the fluence. In the next step, the activity in each voxel is weighted by the efficiency of the corresponding voxel position divided by the total activity. To be able to calculate the efficiency for every position, a high resolution efficiency map was recorded in advance by moving a ^{22}Na point source in 1 mm steps through the detection zone (shown in figure 4) using a mechanical positioning device. This efficiency map is normalized to unity at the detection zone center and can be converted into absolute values by applying the calibration factor measured with the ^{22}Na source right before the measurements (see above). The reduction of the efficiency due to the absorption of one of the 511 keV photons within the target or the detector wrapping and due to positrons escaping from the target is taken into account for each individual voxel by using the photon attenuation coefficients from the NIST XCOM database (Berger *et al* 2010) and by applying a positron loss model based on FLUKA
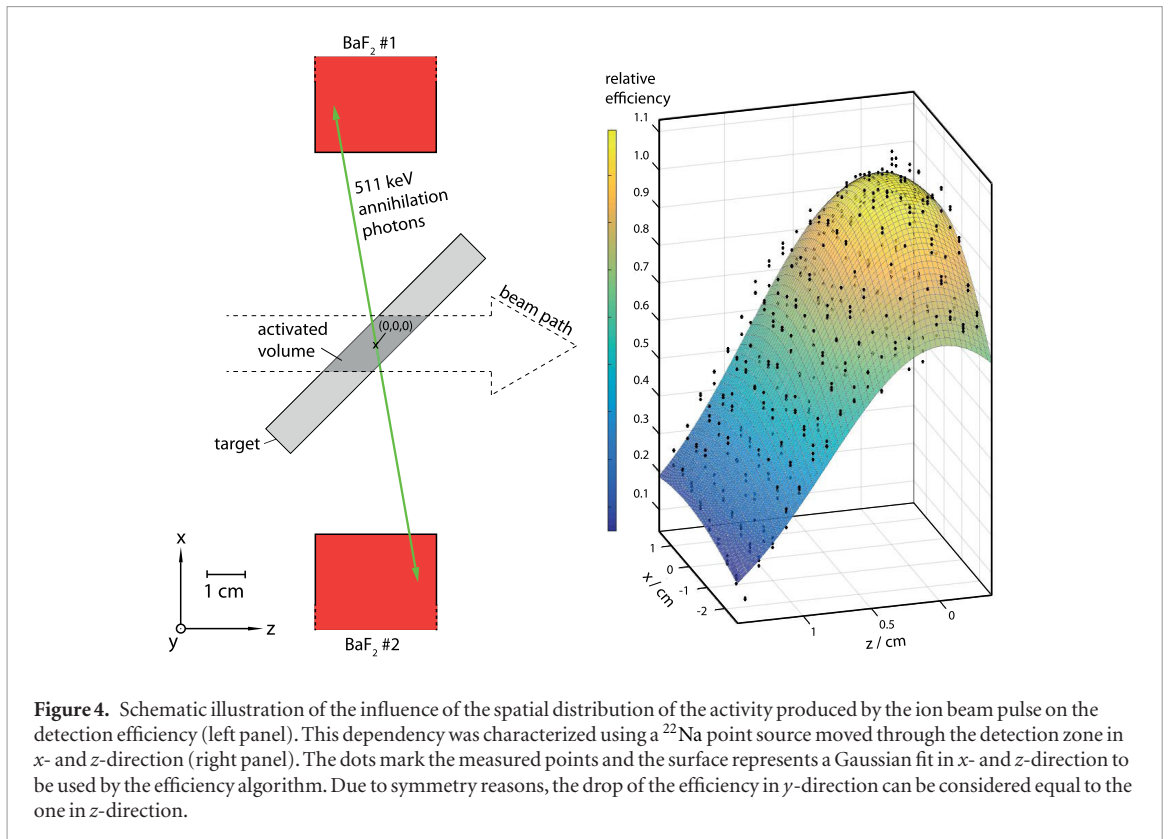
Figure 4. Schematic illustration of the influence of the spatial distribution of the activity produced by the ion beam pulse on the detection efficiency (left panel). This dependency was characterized using a ^{22}Na point source moved through the detection zone in *x*- and *z*-direction (right panel). The dots mark the measured points and the surface represents a Gaussian fit in *x*- and *z*-direction to be used by the efficiency algorithm. Due to symmetry reasons, the drop of the efficiency in *y*-direction can be considered equal to the one in *z*-direction.

simulations (Ferrari *et al* 2005, Böhlen *et al* 2014, Battistoni *et al* 2015, 2016) considering published ^{11}C and ^{15}O positron spectra given by Eckerman *et al* (1994) and a ^{10}C positron spectrum calculated according to a model given by Levin and Hoffman (1999). Finally, the resulting detection efficiency, which relates the measured coincidence rate with the activity for the particular measurement (true 180° coincidences per second per Becquerel) is obtained by averaging the activity-weighted efficiency over all voxels.

Due to the target thicknesses of 3.8 mm for beryllium oxide or 5 and 10 mm for graphite, the efficiency reduction due to positron loss was only in the order of 4%–8% since they could only escape from the last 1–2 mm of the graphite targets (depending on the isotope) and from the last mm of the beryllium oxide targets. The calculated efficiencies varied between 0.30% and 0.65% for the proton measurements and between 0.41% and 0.73% for the carbon ion measurements. The generally very low efficiencies are due to the small solid angle covered by the scintillators and the differences between the measurements at different energies are mainly due to the varying beamspot sizes, which are also the reason for the higher efficiencies for the carbon ion measurements compared to the proton measurements (see figure 3).

2.8. Cross section calculation

The measured 180° coincidence count rate as a function of time $A(t)$ can be fitted by a composite exponential decay function (Stöckmann 1978) (one exponential function for each produced isotope) according to equation (1)

$$A(t) = A_0^{X_1} \cdot 0.5^{\frac{t}{T_{1/2}^{X_1}}} + A_0^{X_2} \cdot 0.5^{\frac{t}{T_{1/2}^{X_2}}} + ...$$
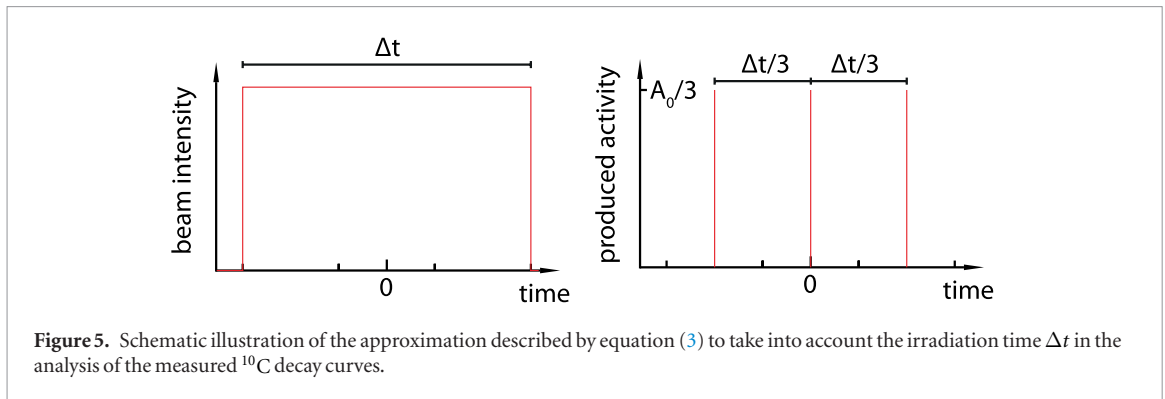
(1)

where $A_0^{X_i}$ are the initial count rates and $T_{1/2}^{X_i}$ are the half lives of the isotopes X_i.

Using the initial count rates obtained from fitting the measured decay curve, the production cross sections σ_{X_i} can be calculated according to equation (2)

$$\sigma^{X_i} = \frac{\frac{A_0^{X_i}}{\epsilon}}{z \cdot \frac{n}{V} \cdot N \cdot \lambda^{X_i}}$$

(2)

where ϵ is the detection efficiency, z is the target thickness in beam direction, n/V is the number of target nuclei per volume, N is the number of primary particles in the beam pulse and λ^{X_i} is the decay constant of isotope X_i.

A fitting function according to equation (1) assumes that the irradiation time Δt is much shorter than the half lives $T_{1/2}$ of the isotopes produced because the competition between build-up and radioactive decay during the irradiation is not taken into account. For isotopes where the duration of the irradiation is non-negligible compared with the half life—in this work this was only the case for ^{10}C—the term for a single isotope can be split

Figure 5. Schematic illustration of the approximation described by equation (3) to take into account the irradiation time Δt in the analysis of the measured ^{10}C decay curves.

into multiple terms having different zero time points. With this approach, the temporal course of the activity production can be taken into account in good approximation. For the fitting model in this work the time point of the ^{10}C production was split into three according to equation (3).

$$A^{^{10}C}(t) = \frac{A_0^{^{10}C}}{3} \cdot 0.5^{\frac{t-\Delta t/3}{T_{1/2}^{^{10}C}}} + \frac{A_0^{^{10}C}}{3} \cdot 0.5^{\frac{t}{T_{1/2}^{^{10}C}}} + \frac{A_0^{^{10}C}}{3} \cdot 0.5^{\frac{t+\Delta t/3}{T_{1/2}^{^{10}C}}}. \tag{3}$$

The approximation described by equation (3) is illustrated in figure 5.

2.9. Uncertainty estimation

The energy loss within the targets smeared the energy where the observed reactions took place. This energy interval was kept small by using thin targets but is non-negligible, especially for the low energy measurement points. It is accounted for by giving each cross section value for the mean energy at the target center with an uncertainty interval covering the energies before and after. These energy uncertainty intervals were calculated by transport calculations through the different targets using the FLUKA code. The initial beam energy spread from the accelerator ($\sim 0.1\%$–1% depending on the energy) was not taken into account because it is negligible compared with the energy loss effects described before.

Besides this energy smearing, there are also different uncertainties to consider that propagate directly into the uncertainty of the cross section value: the activity of the ^{22}Na source used for calibration of the detection system has a manufacturing uncertainty of 3%. The number of primary ions impinging on the target was determined by the monitor IC in the nozzle. Its calibration by means of an absorbed dose to water measurement under dosimetric reference conditions has an uncertainty which was assumed to be 4% (where 2% results from the uncertainty of the k_Q value used for absorbed dose to water determination and another 2% from the beam model which was used to convert the measured absorbed dose to water into fluence). The algorithm used to calculate the detection efficiency considers all relevant effects but uses some simplified models (e.g. the single Gaussian beam profile), therefore the calculated efficiency is not free of uncertainty either. This was estimated to be 3% based on variations of the input parameters within reasonable limits. Following the rules of error propagation, these individual uncertainties add up to an estimated total systematic cross section uncertainty of 10%. Lastly, the produced initial activities are estimated by fitting the measured decay curve with a composite exponential decay function, whose accuracy is mainly affected by the amount of produced activity and the resulting counting statistics. This uncertainty was estimated by the fitter individually for each measurement and added to the generalized systematic uncertainty of 10% given above.

Uncertainties associated with the targets (homogeneity or misplacement) are small against the above mentioned sources of uncertainty and are therefore neglected.

2.10. Proton transport calculation

The measured production cross sections for the main PT-PET isotopes ^{11}C and ^{15}O by protons were validated against published activity profiles measured in a tissue equivalent gel phantom with a clinical PET scanner after proton irradiation (Espana *et al* 2011). For this purpose, look-up tables with the ^{12}C$(\mathrm{p,pn})^{11}$C and ^{16}O$(\mathrm{p,pn})^{15}$O excitation functions representing the measured cross sections presented here were created and convoluted with the proton spectrum to obtain the produced β^+-activity (the method and also how to model the temporal progress of the activity has been described in detail by Parodi *et al* (2002) and Bauer *et al* (2013)).

In this work, the proton spectrum as a function of depth was obtained from simulations with the Monte Carlo toolkit TOPAS (Perl *et al* 2012). The proton source spectrum for the simulation was optimized to reproduce the depth dose profile published in the article of Espana *et al* (2011). The main energy peak was found to lie around 116 MeV as also stated by Espana *et al* (2011) but notably, also a low-energy proton component was required in the input spectrum to reproduce the entrance region of the reference dose profile. This can be explained by

the fact that Espana *et al* (2011) performed their experiment at a passive scattering beamline where secondary protons are produced in the scatter foils. The elemental composition of the phantom material was given as 9.6% H, 14.6% C, 1.46% N and 73.8% O and the density was given as 1.13 g cm^{-3}. Due to the high carbon and oxygen content in the tissue equivalent gel, it is well suited to validate the production cross sections on both target materials. To take account of the PET scanner resolution the calculated activity profiles were convoluted with a Gaussian kernel with 7 mm FWHM, also given by Espana *et al* (2011). The image acquisition protocols used in the experiment should mimic two different PT-PET methods: the 5 min protocol (5 min image acquisition started directly after the irradiation) corresponds to an in-room PET measurement, while the 30 min protocol (30 min image acquisition after a 15 min break) is more similar to an offline PET measurement.

The reaction channels that had to be considered in the transport calculation were ^{12}C$(p, pn)^{11}$C and ^{16}O$(p, pn)^{15}$O which were characterized in the present work, but also ^{16}O$(p, X)^{11}$C and ^{16}O$(p, X)^{13}$N which were not measured in this work. The cross section tables for the latter two channels were taken from Bauer *et al* (2013). Contributions of ^{10}C can be neglected for the acquisition protocols used by Espana *et al* (2011) because also for the 5 min measurement they could not avoid a break of ∼1 min between irradiation stop and start of the PET imaging which is long enough for the majority of the ^{10}C to decay.

3. Results and discussion
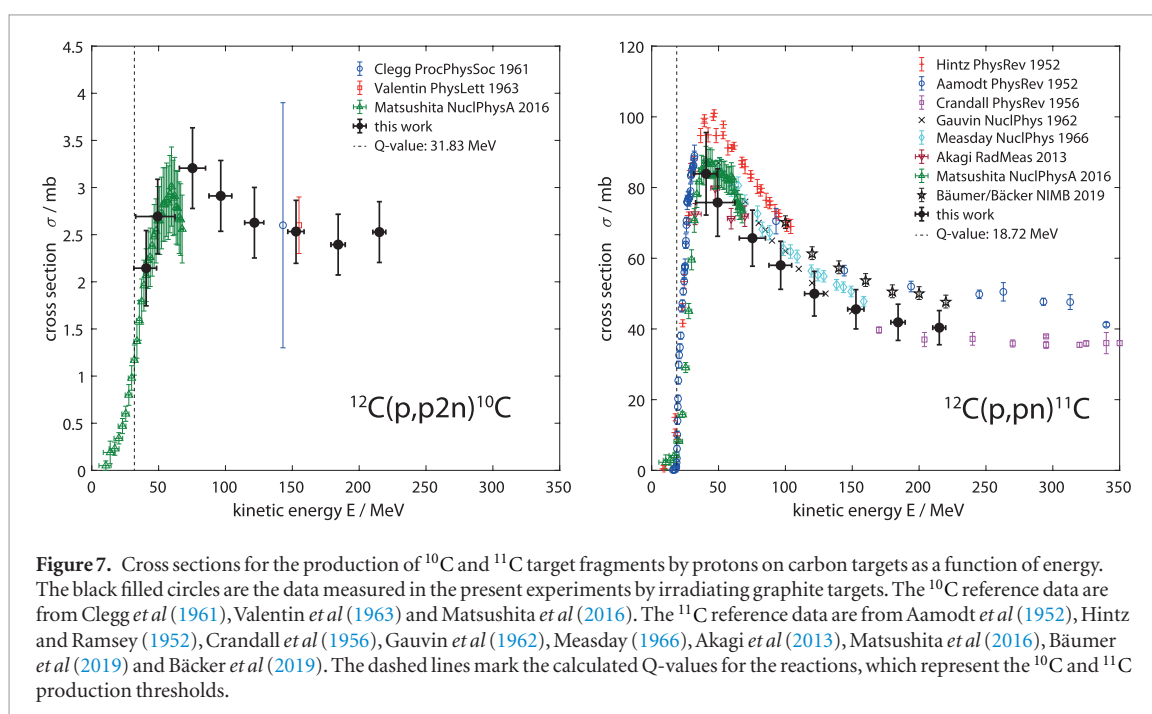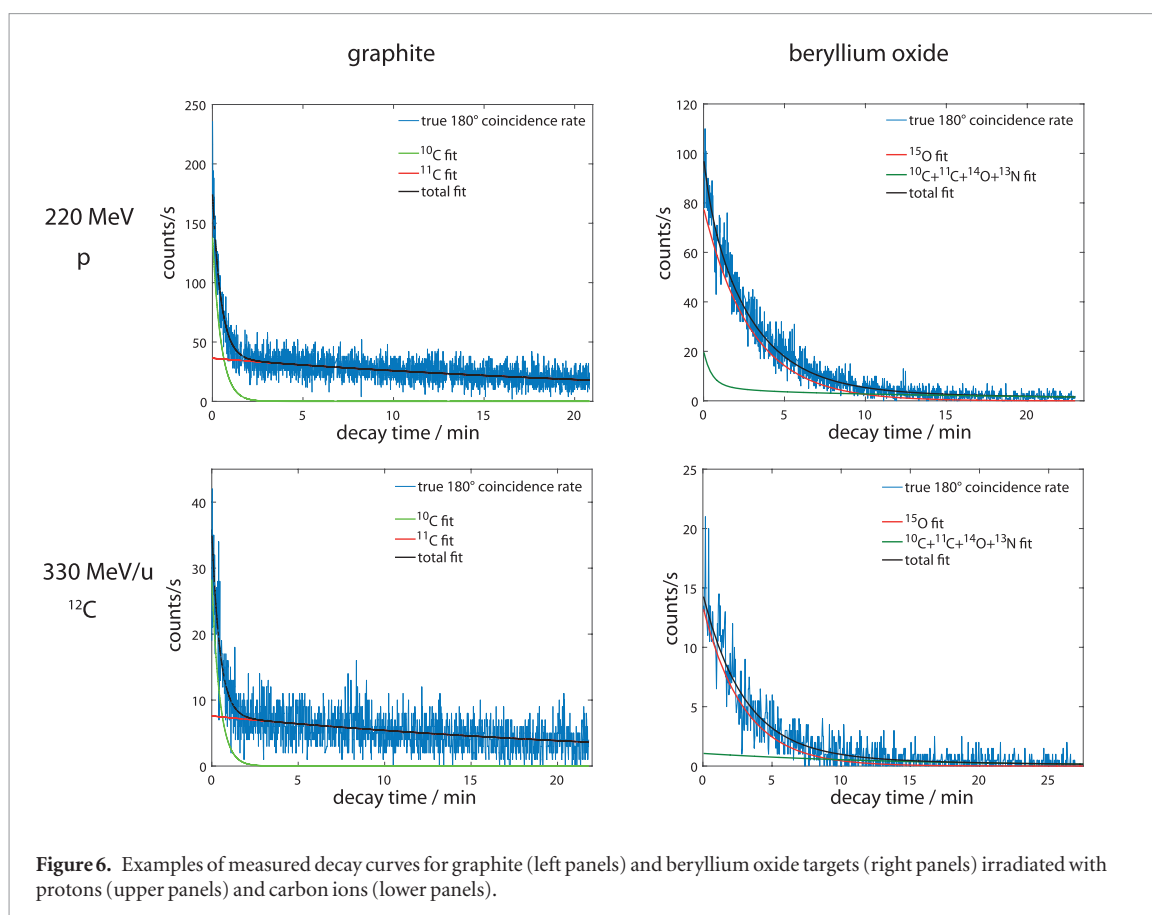
3.1. Measured decay curves

Figure 6 shows the measured decay curves for graphite and beryllium oxide targets irradiated with both protons and carbon ions.

It can be observed that for the graphite targets the activity decreases fast in the first two minutes after irradiation because the short-lived ^{10}C (half life: 19.29 s) dominates the activity while later only the produced ^{11}C (half life: 20.334 min) remains. In contrast to these distinct two decay components, the decay curves of the activated beryllium oxide are dominated by the produced ^{15}O (half life: 122.24 s) and the other produced isotopes (^{10}C, ^{11}C, ^{14}O, ^{13}N) only contribute a few percent to the total activity. It can also be seen, that the produced activity per irradiation pulse was considerably lower for carbon ions than for protons which results in a lower signal to noise ratio (and thus less accurate cross section measurements as seen below). This can be explained by looking at the requirements for the radiotherapy accelerator operated at MIT: in the facility design phase the maximum intensities (ions per second) that need to be extracted from the synchrotron were defined in terms of dose rate. Due to the much higher LET of carbon ions compared to protons, the maximum carbon ion intensity can be a factor of ∼30 lower than the proton intensity and still generate the same dose rate. Also the PET counting statistics that can be collected for range verification during patient treatments with carbon ions suffers from this relation compared to proton therapy (Parodi *et al* 2002). However, in our experiment the lower particle numbers in the carbon ion beam pulses were partially compensated by their larger nuclear reaction cross sections and sharper beamspots (better detection efficiency) compared to protons. Additionally, the carbon ion irradiation times were increased up to twice the length of the proton pulses to further increase the number of primary particles and thereby the amount of produced activity.

3.2. PET isotope production cross sections

The initial activities obtained from the fit functions shown in figure 6 could be converted into the production cross sections by applying equation (2). Figure 7 shows the ^{10}C and ^{11}C production cross sections as a function of energy (*excitation functions*) for protons impinging on carbon targets. For comparison also the Q-values (the energy that is absorbed in a nuclear reaction) for both channels calculated by comparing the masses of the nuclei in the initial and in the final state are shown.

For the ^{12}C$(p, pn)^{11}$C reaction channel, there are a lot of reference data available and the cross section data obtained in the present experiments fit rather well into the general systematics. There is a good agreement between the present data and the reference data from the literature except those from the very early publications by Hintz and Ramsey (1952) and Aamodt *et al* (1952) and the very recent work by Bäumer *et al* (2019) and Bäcker *et al* (2019). While deviations of our recent measurements from values published in the 1950s are not particularly surprising, the deviation from the cross section at 100 MeV reported by Bäumer *et al* (2019) (∼5% from error bar to error bar and ∼17% from value to value) needs more attention and is therefore discussed in the following. The approach to determine the ^{11}C production cross section via the measurement of the amount of induced activity is comparable to our approach. However, the experimental method of Bäumer *et al* (2019) is quite different from the one presented in this work. While our experiment was set up in-beam and the induced β^+ activity was measured with scintillation detectors coupled by a coincidence unit, Bäumer *et al* (2019) transported their irradiated targets from the proton therapy center in Essen to a low background gamma spectrometry facility in Dortmund ∼35 km away to analyze the samples there using a well-characterized high purity germanium detector. They used the same graphite target material type with high purity as used in this

Figure 6. Examples of measured decay curves for graphite (left panels) and beryllium oxide targets (right panels) irradiated with protons (upper panels) and carbon ions (lower panels).

Figure 7. Cross sections for the production of ^{10}C and ^{11}C target fragments by protons on carbon targets as a function of energy. The black filled circles are the data measured in the present experiments by irradiating graphite targets. The ^{10}C reference data are from Clegg *et al* (1961), Valentin *et al* (1963) and Matsushita *et al* (2016). The ^{11}C reference data are from Aamodt *et al* (1952), Hintz and Ramsey (1952), Crandall *et al* (1956), Gauvin *et al* (1962), Measday (1966), Akagi *et al* (2013), Matsushita *et al* (2016), Bäumer *et al* (2019) and Bäcker *et al* (2019). The dashed lines mark the calculated Q-values for the reactions, which represent the ^{10}C and ^{11}C production thresholds.

work, therefore no differences can be expected from the material, but the irradiation fields used are quite different: while in the present work the targets were irradiated with a single pencil beam impinging on the target center, Bäumer *et al* (2019) irradiated their targets with a scanned beam producing a homogeneous fluence on the target. Only slight differences (up to ∼3% according to a dosimetric study by Gomà *et al* (2014)) may originate from the different way of determining the number of primary particles impinging on the target. In this work the clinical monitor calibration determined by an absorbed dose to water measurement under dosimetric reference conditions was used while Bäumer *et al* (2019) did separate measurements with a Faraday cup. The possible origin of the discrepancies between primary particle fluences determined by means of IC measure-
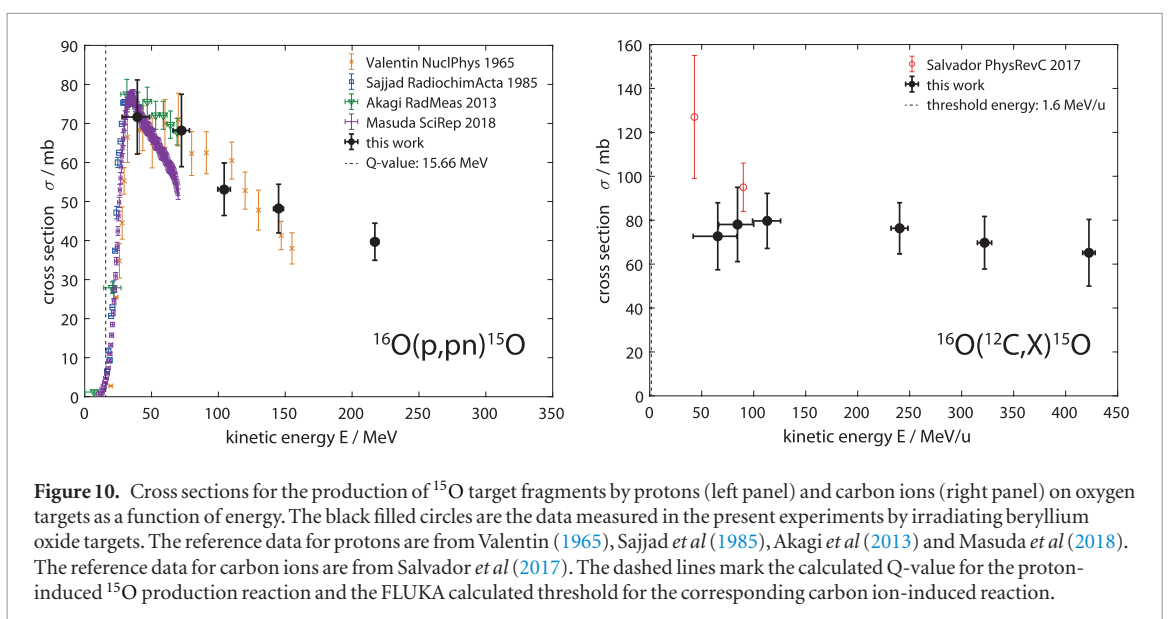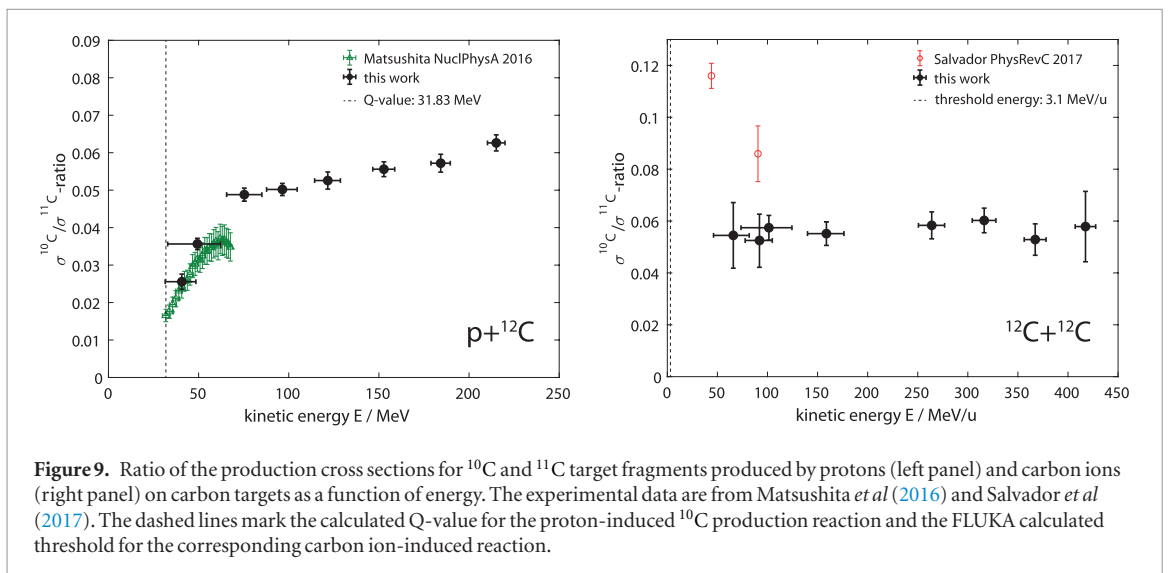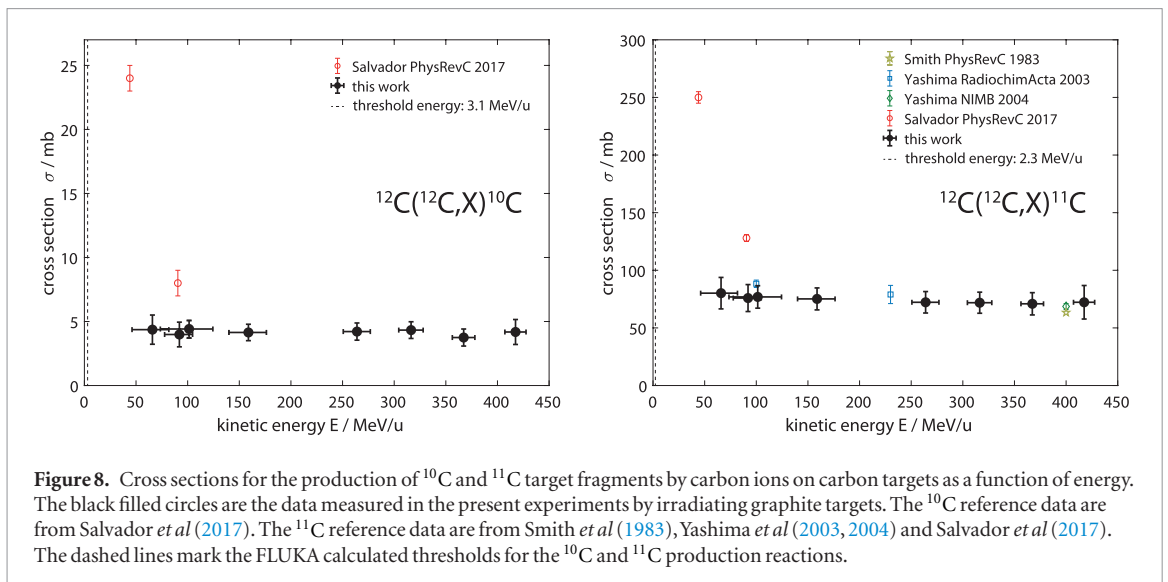
Figure 8. Cross sections for the production of ^{10}C and ^{11}C target fragments by carbon ions on carbon targets as a function of energy. The black filled circles are the data measured in the present experiments by irradiating graphite targets. The ^{10}C reference data are from Salvador *et al* (2017). The ^{11}C reference data are from Smith *et al* (1983), Yashima *et al* (2003, 2004) and Salvador *et al* (2017). The dashed lines mark the FLUKA calculated thresholds for the ^{10}C and ^{11}C production reactions.

Figure 9. Ratio of the production cross sections for ^{10}C and ^{11}C target fragments produced by protons (left panel) and carbon ions (right panel) on carbon targets as a function of energy. The experimental data are from Matsushita *et al* (2016) and Salvador *et al* (2017). The dashed lines mark the calculated Q-value for the proton-induced ^{10}C production reaction and the FLUKA calculated threshold for the corresponding carbon ion-induced reaction.

Figure 10. Cross sections for the production of ^{15}O target fragments by protons (left panel) and carbon ions (right panel) on oxygen targets as a function of energy. The black filled circles are the data measured in the present experiments by irradiating beryllium oxide targets. The reference data for protons are from Valentin (1965), Sajjad *et al* (1985), Akagi *et al* (2013) and Masuda *et al* (2018). The reference data for carbon ions are from Salvador *et al* (2017). The dashed lines mark the calculated Q-value for the proton-induced ^{15}O production reaction and the FLUKA calculated threshold for the corresponding carbon ion-induced reaction.

Table 1. Measured cross sections for the production of ^{10}C and ^{11}C target fragments by protons and carbon ions on carbon targets.

Projectile	Target	Thickness / mm	Kinetic energy / MeV u^{-1}	^{10}C production cross section $\sigma^{^{10}C}$ / mb	^{11}C production cross section $\sigma^{^{11}C}$ / mb
p	^{12}C	9.91	$215.1^{+4.8}_{-4.9}$	2.53 ± 0.33	40.4 ± 4.8
p	^{12}C	9.90	$184.3^{+5.3}_{-5.4}$	2.40 ± 0.33	41.9 ± 5.1
p	^{12}C	9.91	$152.8^{+6.0}_{-6.2}$	2.53 ± 0.34	45.6 ± 5.6
p	^{12}C	9.85	$121.7^{+7.0}_{-7.3}$	2.63 ± 0.38	50.0 ± 6.3
p	^{12}C	9.83	$96.5^{+8.2}_{-8.8}$	2.91 ± 0.38	58.0 ± 6.8
p	^{12}C	9.91	$75.4^{+9.6}_{-9.8}$	3.21 ± 0.43	65.7 ± 7.9
p	^{12}C	9.83	$49.3^{+12.9}_{-16.5}$	2.69 ± 0.40	75.8 ± 9.6
p	^{12}C	4.99	$40.7^{+7.8}_{-9.2}$	2.15 ± 0.41	83.4 ± 11.7
^{12}C	^{12}C	9.91	$417.5^{+10.2}_{-10.3}$	4.18 ± 0.99	72.3 ± 14.5
^{12}C	^{12}C	9.90	$367.3^{+10.8}_{-11.0}$	3.75 ± 0.67	70.9 ± 9.7
^{12}C	^{12}C	9.91	$316.4^{+11.7}_{-11.9}$	4.33 ± 0.66	71.9 ± 9.2
^{12}C	^{12}C	9.91	$264.0^{+12.9}_{-13.3}$	4.21 ± 0.68	72.2 ± 9.3
^{12}C	^{12}C	9.91	$158.8^{+17.4}_{-18.9}$	4.15 ± 0.65	75.2 ± 9.5
^{12}C	^{12}C	9.90	$101.4^{+23.0}_{-27.9}$	4.42 ± 0.69	76.9 ± 9.8
^{12}C	^{12}C	5.01	$92.0^{+12.8}_{-14.3}$	3.99 ± 0.99	75.9 ± 11.7
^{12}C	^{12}C	4.99	$65.9^{+15.9}_{-19.7}$	4.37 ± 1.17	80.2 ± 13.7

Table 2. Measured cross sections for the production of ^{15}O target fragments by protons and carbon ions on oxygen targets.

Projectile	Target	Thickness / mm	Kinetic energy / MeV u^{-1}	^{15}O production cross section $\sigma^{^{15}O}$ / mb
p	^{16}O	3.93	$217.0^{+2.8}_{-2.9}$	39.7 ± 4.8
p	^{16}O	3.92	$145.0^{+3.7}_{-3.8}$	48.2 ± 6.3
p	^{16}O	3.91	$104.2^{+4.6}_{-4.8}$	53.2 ± 6.8
p	^{16}O	3.88	$72.4^{+6.0}_{-6.4}$	68.2 ± 9.4
p	^{16}O	3.91	$39.4^{+9.1}_{-11.4}$	71.7 ± 9.6
^{12}C	^{16}O	3.92	$422.4^{+5.9}_{-6.0}$	65.1 ± 15.4
^{12}C	^{16}O	3.91	$322.0^{+6.8}_{-6.9}$	69.8 ± 12.2
^{12}C	^{16}O	3.88	$240.3^{+8.0}_{-8.2}$	76.4 ± 11.8
^{12}C	^{16}O	3.82	$113.0^{+12.9}_{-14.0}$	79.7 ± 12.7
^{12}C	^{16}O	3.91	$84.5^{+15.6}_{-18.1}$	78.0 ± 17.2
^{12}C	^{16}O	3.90	$65.5^{+18.3}_{-23.6}$	72.7 ± 15.5

ments and Faraday cup measurements has been widely discussed (Palmans and Vanitsky 2016, Gomà *et al* 2016) and it is still not finally resolved which method gives the more accurate result. Therefore, a conservative estimate on the accuracy of the IC based monitor calibration is included in our uncertainty calculation (see above). The origin of the remaining discrepancy between the ^{11}C production cross sections determined in the present experiment and that of Bäumer *et al* (2019) are not clear yet and could be investigated in future work.

The ^{12}C(p, p2n)^{10}C reaction channel has been less investigated in previous studies than the channel for ^{11}C production, however, there is also reasonable agreement between the ^{10}C production cross sections presented here and the few data available in the literature. The decrease to higher energies measured by Matsushita *et al* (2016) might be an edge artifact due to their experimental method (PET imaging of thick targets after irradiation). Also the fact that they measured ^{10}C production cross section values greater than zero below the Q-value of the reaction is probably an artifact because they obtained their energy information by correlation of the induced activity with the depth in their target. However, this relation is strongly smeared at high depths by the energy loss straggling.

Figure 8 shows the ^{10}C and ^{11}C production cross sections as a function of energy for carbon ions impinging on carbon targets. In the case of carbon projectiles the simple calculation of a single Q-value is not sufficient to describe the reaction threshold appropriately due to the several different projectile fragmentation channels that are possible. Therefore, the reaction thresholds shown in figure 8 were calculated using an appropriate built-in FLUKA routine that returns the corresponding energy threshold for each fragmentation channel. The minimum energy threshold among all possible fragmentation channels is used here as reaction threshold. However, it is

important to note that unless complete fusion occurs, usually not all nucleons take part in a nucleus-nucleus reaction, and therefore the required energy per nucleon is actually greater for most of the collision processes than that given by the reaction threshold. Moreover, due to its not clear and straightforward determination, the Coulomb barrier has not been considered in the calculation of the reaction thresholds. Therefore, the values shown in figure 8 should only be used as a rough indicator of the actual minimum energy per nucleon needed for the reaction to occur.

The available data for target fragmentation induced by carbon projectiles is much more sparse than for protons. The few datapoints from experiments at the Bevalac (Smith *et al* 1983) and at the HIMAC accelerator (Yashima *et al* 2003, 2004) compare reasonably well with the present cross sections while the newer datapoints from Salvador *et al* (2017) lie significantly higher. In contrast to the proton data (see figure 7), no rise of the ^{10}C and ^{11}C production cross sections on ^{12}C targets towards lower energies can be observed for incident carbon ions in the energy range investigated in this work.

Figure 9 shows the same data as figures 7 and 8, but as the ratio of the ^{10}C and ^{11}C production cross sections both for protons (left panel) and carbon ions (right panel) impinging on carbon targets as a function of energy.

Most of the systematic uncertainties cancel out when calculating the ratio, therefore the error bars are considerably smaller than in figures 7 and 8. However, the remaining uncertainties due to the counting statistics are larger for the carbon ion measurements than for the proton measurements due to the lower beam intensities (see above). A comparison with literature data is only possible for experiments where ^{10}C and ^{11}C production were measured simultaneously. This is only the case for the datasets from Matsushita *et al* (2016) and Salvador *et al* (2017). The present proton data compare reasonably well with those by Matsushita *et al* (2016) (their values below the Q-value of 31.83 MeV are not shown, see discussion above) while for carbon ions the ratios presented here are again lower than those reported by Salvador *et al* (2017). For protons, the two-neutron-removal reaction cross section (^{10}C production) relative to the cross section for removal of only one neutron (^{11}C production) decreases with decreasing energy while for carbon projectiles, no energy-dependency could be observed at all in the investigated energy range of this study (down to $\sim$75 MeV u^{-1}).

Figure 10 shows the ^{15}O production cross section as a function of energy for protons and carbon ions impinging on oxygen targets.

For the ^{16}O(p, pn)^{15}O reaction channel, the measured dataset fits well into the literature data and extends them towards higher energies. For the corresponding carbon ion reaction, there is fair agreement with the higher energy datapoint by Salvador *et al* (2017) but again (see also figure 8) the rise of the cross section towards lower energies which they report could not be reproduced in the present experiment. Their experimental method is comparable to our approach (monitoring of the 511 keV photon emission with a pair of scintillators and a coincidence logic), but they do not report about any random coincidence correction. However, as shown in figure 2, without this correction the produced activity of the generated isotopes and consequently their production cross sections may be overestimated (depending on the produced activity). Therefore, one could speculate that the discrepancy between the cross sections reported by Salvador *et al* (2017) and the values presented here could be due to a missing correction for random coincidences in the method by Salvador *et al* (2017). Another point where their experiment and the measurements presented in this work differ considerably is the method how the beam energy was varied: while at MIT the energy could be actively changed by the synchrotron, Salvador *et al* (2017) had to use degrader plates which introduces the issue that the beam gets already contaminated by fragments before hitting the target. Another point where their method differs from the one presented here is that their target had to be moved to the measurement position after the irradiation while our setup could measure in-beam. Further research or comparisons could help to clarify where exactly these differences come from.
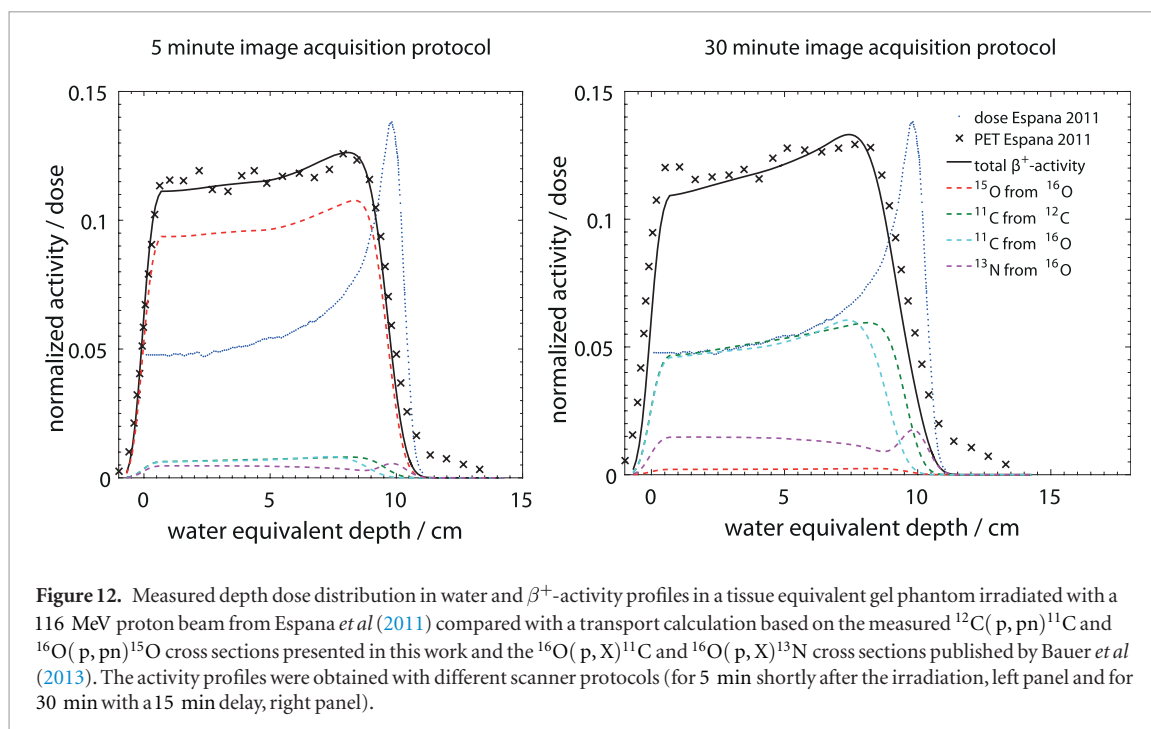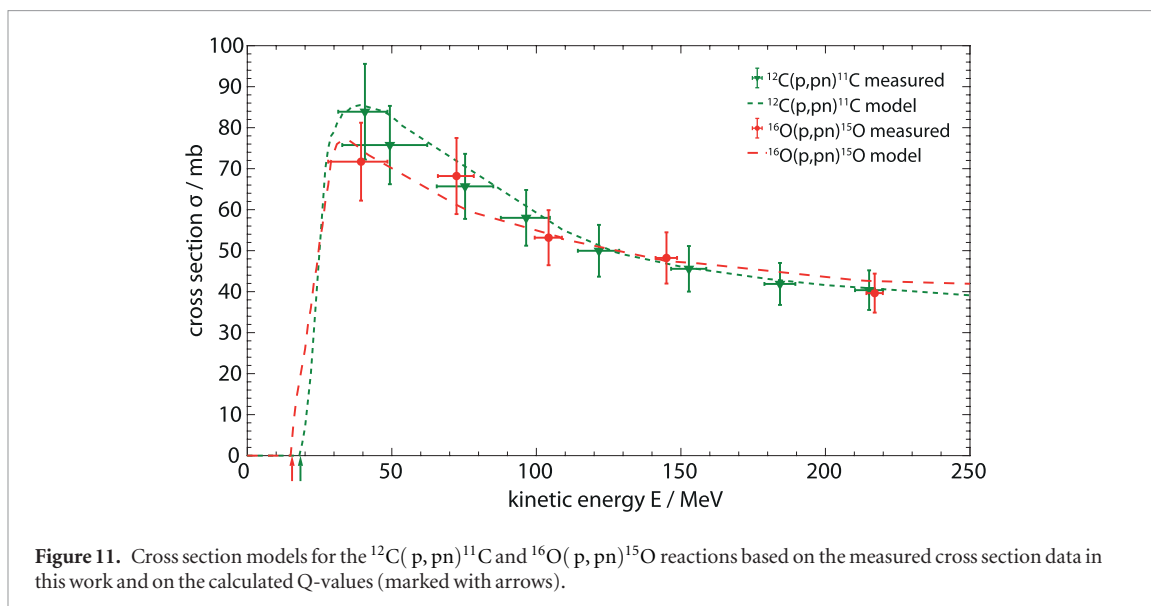
Generally, the threshold energies (expressed in MeV u^{-1}) are considerably lower for the carbon ion reactions than for the proton-induced reactions. For protons this leads to a gap of $\sim$2–5 mm between the end of the activity profiles and the Bragg peak (Parodi *et al* 2002), while carbon ions produce target fragments almost until the end of their range. Thus for carbon ions there is a clear range correlation not only in the β^+-activity profiles of the ^{10}C and ^{11}C projectile fragments (due to kinematics they stop shortly before the primary ^{12}C range (Enghardt *et al* 1999)) but also in those of the ^{10}C, ^{11}C and ^{15}O target fragments created along the beam path.

The cross section data presented in figures 7, 8 and 10 are also compiled in tables 1 and 2.

3.3. Proton transport calculation

Figure 11 shows the cross section models for the ^{12}C(p, pn)^{11}C and ^{16}O(p, pn)^{15}O reactions used for the radiation transport calculation. The calculated Q-values (see figures 7 and 10) were assumed as reaction thresholds. For sake of clarity the reference data from the literature which were also used as guidance for the models are not shown in figure 11.

The results of the proton transport calculation using the ^{12}C(p, pn)^{11}C and ^{16}O(p, pn)^{15}O cross sections presented in this work and the ^{16}O(p, X)^{11}C and ^{16}O(p, X)^{13}N cross sections published by Bauer *et al*

Figure 11. Cross section models for the ^{12}C(p,pn)^{11}C and ^{16}O(p,pn)^{15}O reactions based on the measured cross section data in this work and on the calculated Q-values (marked with arrows).

Figure 12. Measured depth dose distribution in water and β^+-activity profiles in a tissue equivalent gel phantom irradiated with a 116 MeV proton beam from Espana *et al* (2011) compared with a transport calculation based on the measured ^{12}C(p,pn)^{11}C and ^{16}O(p,pn)^{15}O cross sections presented in this work and the ^{16}O(p,X)^{11}C and ^{16}O(p,X)^{13}N cross sections published by Bauer *et al* (2013). The activity profiles were obtained with different scanner protocols (for 5 min shortly after the irradiation, left panel and for 30 min with a 15 min delay, right panel).

(2013) are shown in figure 12. The calculated profiles are compared with profiles measured with a PET scanner (Espana *et al* 2011). The depth in the tissue equivalent gel phantom was converted into water equivalent depth with a conversion factor determined by TOPAS simulations. Considering the noise in the measured activity profiles their shapes are well reproduced for both irradiation protocols (the 5 min protocol being dominated by ^{15}O, and the 30 min protocol being dominated by ^{11}C) by the transport calculation using the cross section tables shown in figure 11. This is in contrast to the original work by Espana *et al* (2011) where standard ICRU and EXFOR tables were applied and none of them could reproduce both the ^{11}C and ^{15}O profiles accurately. As already pointed out by Espana *et al* (2011) the tails behind the distal edges of the measured activity profiles are artifacts due to background noise and PET image reconstruction and can therefore be neglected. As seen in comparison with the dose profiles the distal edges of the activity profiles lie some mm before the distal edge of the Bragg curve. This shift is well-known and is due to the threshold energies of the reactions producing the β^+-emitters (see also figures 7 and 10).

This example shows that the calculation of activity depth profiles for protons does not require a full Monte Carlo simulation but only the proton spectrum as a function of depth (which is e.g. available in typical treatment planning systems as basic data) because the created target fragments do not need to be transported. For this kind of calculations cross section tables can be generated using the cross section data presented in this work and the respective Q-values. However, in the case of carbon ions, the projectile fragments are produced with velocities

similar to the projectiles and therefore also need to be transported by the code used for calculation of the reference pattern. This is more complex and a typical problem where at least a partial (Pönisch *et al* 2004) or even a full Monte Carlo simulation (Sommerer *et al* 2009) is required.

4. Conclusion

Activation experiments with protons and carbon ions were performed at the MIT with the aim to study the production of PET isotopes (^{10}C, ^{11}C and ^{15}O) on carbon and oxygen targets. The cross section data set obtained during these experiments is relevant for the validation and optimization of heavy ion transport codes used for PET range verification (e.g. Monte Carlo codes like FLUKA).

For the reaction channels which have been well-characterized in previous studies (e.g. ^{12}C(p, pn)^{11}C) the present cross sections fit well into the systematics of the literature data. This underpins the validity of the present data for channels that have been less investigated in the past. Especially the carbon ion data provided in this work will help to refine the corresponding nuclear reaction models. For a final validation of the optimized nuclear models, the transport calculations can then be compared with thick target activation yields and profiles measured with a PET scanner as demonstrated in section 3.3 but also done by e.g. Parodi *et al* (2002, 2005), Bauer *et al* (2013) or Hofmann *et al* (2019).

The validation and optimization of the nuclear reaction models embedded in the FLUKA Monte Carlo code based on the cross section data presented in this work are already ongoing. For protons the measured data are reproduced quite well by the FLUKA models (the ^{12}C(p, pn)^{11}C and ^{16}O(p, pn)^{15}O cross sections in FLUKA can be found in Battistoni *et al* (2016)) while for carbon projectiles some model refinements are necessary. These adjustments, which will be subject of future work, will have a direct clinical relevance since FLUKA is used as reference at CNAO where an in-beam PET is available for verification of proton and carbon ion treatments (Fiorina *et al* 2016, 2018).

The production cross sections for the lighter β^+-emitters among the ^{16}O fragments (^{10}C, ^{11}C, ^{13}N, ^{14}O) that could not be distinguished in the experimental data collected in the present work may be measured by using beams of higher intensity and longer recording times. Higher intensity beams would also increase the produced activity and therefore further decrease the cross section uncertainties for the isotopes reported in this work. Future experiments could extend the present study to lower energies and also the production of PET isotopes by other ions that are considered to be used for radiotherapy (e.g. ^{4}He or ^{16}O) may be interesting to investigate. For bone tissues, also the production cross sections for β^+-emitters on ^{40}Ca targets (e.g. ^{38}K) would be interesting to measure. Precise measurements of the cross sections for fragmentation into non-β^+-emitters (e.g. ^{7}Be) could also be useful for nuclear model optimization.

Acknowledgments

ORCID iDs

Klemens Zink ● https://orcid.org/0000-0001-5785-4101

References

Aamodt R L, Peterson V and Phillips R 1952 C^{12}(p, pn)C^{11} cross section from threshold to 340 MeV *Phys. Rev.* **88** 739–44
Akagi T, Yagi M, Yamashita T, Murakami M, Yamakawa Y, Kitamura K, Ogura K, Kondo K and Kawanishi S 2013 Experimental study for the production cross sections of positron emitters induced from ^{12}C and ^{16}O nuclei by low-energy proton beams *Radiat. Meas.* **59** 262–9
Bäcker C M *et al* 2019 Measurement of nuclear activation cross sections of protons on natural carbon for proton beam energies between 100 and 220 MeV *Nucl. Instrum. Methods Phys. Res.* B **454** 50–5
Battistoni G *et al* 2016 The FLUKA code: an accurate simulation tool for particle therapy *Frontiers Oncol.* **6** 116
Battistoni G *et al* 2015 Overview of the FLUKA code *Ann. Nucl. Energy* **82** 10–8
Bauer J, Unholtz D, Kurz C and Parodi K 2013 An experimental approach to improve the Monte Carlo modelling of offline PET/CT-imaging of positron emitters induced by scanned proton beams *Phys. Med. Biol.* **58** 5193–213

Bäumer C *et al* 2019 Measurement of absolute activation cross sections from carbon and aluminum for proton therapy *Nucl. Instrum. Methods Phys. Res.* B **440** 75–81

Bennett G W, Goldberg A C, Levine G S, Guthy J, Balsamo J and Archambeau J O 1975 Beam localization via ^{15}O activation in proton-radiation therapy *Nucl. Instrum. Methods* **125** 333–8

Berger M J, Hubbell J H, Seltzer S M, Chang J, Coursey J S, Sukumar R, Zucker D S and Olsen K 2010 XCOM: photon cross sections database *NIST Standard Reference Database 8 (XGAM)*

Böhlen T T, Cerutti F, Chin M P W, Fassò A, Ferrari A, Ortega P G, Mairani A, Sala P R, Smirnov G and Vlachoudis V 2014 The FLUKA code: developments and challenges for high energy and medical applications *Nucl. Data Sheets* **120** 211–4

Clegg A B, Foley K J, Salmon G L and Segel R E 1961 Gamma radiation from the medium energy proton bombardment of lithium, beryllium, boron, carbon and nitrogen *Proc. Phys. Soc.* **78** 681

Combs S E, Bauer J, Unholtz D, Kurz C, Welzel T, Habermehl D, Haberer T, Debus J and Parodi K 2012 Monitoring of patients treated with particle therapy using positron-emission-tomography (PET): the MIRANDA study *BMC Cancer* **12** 1–6

Crandall W E, Millburn G P, Pyle R V and Birnbaum W 1956 C^{12}(x; xn)C^{11} and Al^{27}(x; x2pn)Na^{24} cross sections at high energies *Phys. Rev.* **101** 329–37

Durante M and Paganetti H 2016 Nuclear physics in particle therapy: a review *Rep. Prog. Phys.* **79** 59

Eckerman K F, Westfall R J, Ryman J C and Cristy M 1994 Availability of nuclear decay data in electronic form, including beta spectra not previously published *Health Phys.* **67** 338–45

Enghardt W, Crespo P, Fiedler F, Hinz R, Parodi K, Pawelke J and Pönisch F 2004 Charged hadron tumour therapy monitoring by means of PET *Nucl. Instrum. Methods Phys. Res.* A **525** 284–8

Enghardt W, Debus J, Haberer T, Hasch B G, Hinz R, Jäkel O, Krämer M, Lauckner K, Pawelke J and Pönisch F 1999 Positron emission tomography for quality assurance of cancer therapy with light ion beams *Nucl. Phys.* A **654** 1047c–50c

Espana S, Zhu X, Daartz J, Fakhri G E, Bortfeld T and Paganetti H 2011 The reliability of proton-nuclear interaction cross-section data to predict proton-induced PET images in proton therapy *Phys. Med. Biol.* **56** 2687–98

Ferrari A, Sala P R, Fassò A and Ranft J 2005 FLUKA: a multi-particle transport code *CERN-2005-10*

Fiorina E *et al* 2016 An integrated system for the online monitoring of particle therapy treatment accuracy *Nucl. Instrum. Methods Phys. Res.* A **824** 198–201

Fiorina E *et al* 2018 Monte Carlo simulation tool for online treatment monitoring in hadrontherapy with in-beam PET: a patient study *Phys. Medica* **51** 71–80

Gauvin H, Lefort M and Tarrago X 1962 Émission d'hélions dans les réactions de spallation *Nucl. Phys.* **39** 447–63

Gomà C, Lorentini S, Meer D and Safai S 2014 Proton beam monitor chamber calibration *Phys. Med. Biol.* **59** 4961–71

Gomà C, Lorentini S, Meer D and Safai S 2016 Reply to comment on 'Proton beam monitor chamber calibration' *Phys. Med. Biol.* **61** 6594–601

Gwosch K, Hartmann B, Jakubek J, Granja C, Soukup P, Jäkel O and Martisikova M 2013 Non-invasive monitoring of therapeutic carbon ion beams in a homogeneous phantom by tracking of secondary ions *Phys. Med. Biol.* **58** 3755–73

Henriquet P *et al* 2012 Interaction vertex imaging (IVI) for carbon ion therapy monitoring: a feasibility study *Phys. Med. Biol.* **57** 4655

Hintz N M and Ramsey N F 1952 Excitation functions to 100 MeV *Phys. Rev.* **88** 19–27

Hofmann T *et al* 2019 Dose reconstruction from PET images in carbon ion therapy: a deconvolution approach *Phys. Med. Biol.* **64** 025011

Hueso-Gonzalez F, Rabe M, Ruggieri T A, Bortfeld T and Verburg J M 2018 A full-scale clinical prototype for proton range verification using prompt gamma-ray spectroscopy *Phys. Med. Biol.* **63** 185019

Knopf A C and Lomax A 2013 *In vivo* proton range verification: a review *Phys. Med. Biol.* **58** R131–60

Levin C S and Hoffman E J 1999 Calculation of positron range and its effect on the fundamental limit of positron emission tomography system spatial resolution *Phys. Med. Biol.* **781–99** 781–99

Lühr A *et al* 2014 Dependence of simulated positron emitter yields in ion beam cancer therapy on modeling nuclear fragmentation *Appl. Radiat. Isot.* **83** 165–70

Masuda T, Kataoka J, Arimoto M, Takabe M, Nishio T, Matsushita K, Miyake T, Yamamoto S, Inaniwa T and Toshito T 2018 Measurement of nuclear reaction cross sections by using Cherenkov radiation toward high-precision proton therapy *Sci. Rep.* **8** 2570

Matsushita K, Nishio T, Tanaka S, Tsuneda M, Sugiura A and Ieki K 2016 Measurement of proton-induced target fragmentation cross sections in carbon *Nucl. Phys.* A **946** 163–4

Measday D F 1966 The ^{12}C(p; pn)^{11}C Reaction from 50 to 160 MeV *Nucl. Phys.* **78** 476–80

Min C H and Kim C H 2006 Prompt gamma measurements for locating the dose falloff region in the proton therapy *Appl. Phys. Lett.* **89** 183517

Muraro S *et al* 2016 Monitoring of hadrontherapy treatments by means of charged particle detection *Frontiers Oncol.* **6** 1–17

Newhauser W D and Zhang R 2015 The physics of proton therapy *Phys. Med. Biol.* **60** R155–209

Nichols A L and Capote R 2014 Nuclear data for medical applications—recent developments and future requirements *Nucl. Data Sheets* **120** 239–41

Nishio T, Miyatake A, Ogino T, Nakagawa K, Saijo N and Esumi H 2010 The development and clinical use of a beam ON-LINE PET system mounted on a rotating gantry port in proton therapy *Int. J. Rad. Oncol. Biol. Phys.* **76** 277–86

Palmans H and Vanitsky S M 2016 Comment on 'Proton beam monitor chamber calibration' *Phys. Med. Biol.* **61** 6585–93

Parodi K and Polf J C 2018 *In vivo* range verification in particle therapy *Med. Phys.* **45** e1037–50

Parodi K, Enghardt W and Haberer T 2002 In-beam PET measurements of β^{+} radioactivity induced by proton beams *Phys. Med. Biol.* **47** 21–36

Parodi K *et al* 2007 Patient study of *in vivo* verification of beam delivery and range, using positron emission tomography and computed tomography imaging after proton therapy *Int. J. Rad. Oncol. Biol. Phys.* **68** 920–34

Parodi K, Pönisch F and Enghardt W 2005 Experimental study on the feasibility of in-beam PET for accurate monitoring of proton therapy *IEEE Trans. Nucl. Sci.* **52** 778–86

Perl J, Shin J, Schuemann J, Faddegon B and Paganetti H 2012 TOPAS: an innovative proton Monte Carlo platform for research and clinical applications *Med. Phys.* **39** 6818–37

Piersanti L *et al* 2014 Measurement of charged particle yields from PMMA irradiated by a 220 MeV u^{-1} ^{12}C beam *Phys. Med. Biol.* **59** 8483

Pönisch F, Parodi K, Hasch B G and Enghardt W 2004 The modelling of positron emitter production and PET imaging during carbon ion therapy *Phys. Med. Biol.* **49** 5217–32

Richter C *et al* 2016 First clinical application of a prompt gamma based *in vivo* proton range verification system *Radiother. Oncol.* **118** 232–7

Sajjad M, Lambrecht R M and Wolf A P 1985 Cyclotron isotopes and radiopharmaceuticals: XXXVI investigation of some excitation functions for the preparation of ^{15}O, ^{13}N and ^{11}C *Radiochim. Acta* **38** 57–64

Salvador S, Colin J, Cussol D, Divay C, Fontbonne J M and Labalme M 2017 Cross section measurements for production of positron emitters for PET imaging in carbon therapy *Phys. Rev. C* **95** 044607

Schardt D, Elsässer T and Schulz-Ertner D 2010 Heavy-ion tumor therapy: physical and radiobiological benefits *Rev. Mod. Phys.* **82** 383–425

Smeets J *et al* 2012 Prompt gamma imaging with a slit camera for real-time range control in proton therapy *Phys. Med. Biol.* **57** 3371–405

Smith A R, McCaslin J B, Geaga J V, Hill J C and Vary J P 1983 Cross sections for the production of ^{11}C in C targets by ^{12}C at relativistic energies *Phys. Rev. C* **28** 1614–7

Sommerer F, Cerutti F, Parodi K, Ferrari A, Enghardt W and Aiginger H 2009 In-beam PET monitoring of mono-energetic ^{16}O and ^{12}C beams: experiments and FLUKA simulations for homogeneous targets *Phys. Med. Biol.* **54** 3979–96

Stöckmann H J 1978 A new method to analyse composite exponential decay curves *Nucl. Instrum. Methods* **150** 273–81

Testa E, Bajard M, Chevallier M, Dauvergne D, Foulher F L, Freud N, Letang J M, Poizat J C, Ray C and Testa M 2009 Dose profile monitoring with carbon ions by means of prompt-gamma measurements *Nucl. Instrum. Methods Phys. Res.* B **267** 993–6

Tobias C A, Chatterjee A and Smith A R 1971 Radioactive fragmentation of N^{7+} ion beam observed in beryllium target *Phys. Lett.* **37A** 119–20

Valentin L 1965 Réactions (p,n) et (p,pn) induites à moyenne énergie sur des noyaux légers *Nucl. Phys.* **62** 81–102

Valentin L, Albouy G, Cohen J P and Gusakow M 1963 Reactions induites par des protons de 155 MeV sur des noyaux legers *Phys. Lett.* **7** 163–4

Yashima H, Uwamino Y, Iwase H, Sugita H, Nakamura T, Ito S and Fukumura A 2003 Measurement and calculation of radioactivities of spallation products by high-energy heavy ions *Radiochim. Acta* **91** 689–96

Yashima H, Uwamino Y, Iwase H, Sugita H, Nakamura T, Ito S and Fukumura A 2004 Cross sections for the production of residual nuclides by high-energy heavy ions *Nucl. Instrum. Methods Phys. Res.* B **226** 243–63

Zhu X, Espana S, Daartz J, Liebsch N, Ouyang J, Paganetti H, Bortfeld T R and Fakhri G E 2011 Monitoring proton radiation therapy with in-room PET imaging *Phys. Med. Biol.* **56** 4041–57